The scaffold protein PRR14L links the PP2A-TACC3 axis to mitotic fidelity and sensitivity to MPS1 inhibition

Albert Z. Liu[1,2], Akshay Narkar[1], Keming Li[2], Thierry Bertomeu[3], Blake A. Johnson[1], Jasmin Coulombe-Huntington[4], Yi Dong[1], Jin Zhu[2], Mike Tyers[5,6], Rong Li[1,2,7]

1. Department of Cell Biology, Johns Hopkins School of Medicine, Baltimore, MD 21205, USA
2. Mechanobiology Institute, National University of Singapore, Singapore 117411, Singapore
3. The ChemoGenix CRISPR screening facility of the Institute for Research in Immunology and Cancer, University of Montreal, 2950 Chemin de Polytechnique, Montréal, QC H3T 1J4, Canada
4. Department of Bioengineering, McGill University, Montreal, QC H3A 0E9, Canada
5. Department of Molecular Genetics, University of Toronto; Toronto, Ontario M5S 1A8, Canada
6. Program in Molecular Medicine, Peter Gilgan Centre for Research and Learning, The Hospital for Sick Children, Toronto, ON M5G 0A4, Canada
7. Department of Biological Sciences, National University of Singapore, Singapore 117558, Singapore

*Correspondence and lead contact: Rong Li (mbihead@nus.edu.sg)

Abstract

Aneuploidy is a hallmark of cancer and is a potential vulnerability that can be selectively targeted. To systematically identify genes that affect the incidence and fitness of aneuploid cells, we conducted a genome-wide CRISPR/Cas9 screen using NMS-P715, an inhibitor of the spindle assembly checkpoint (SAC) kinase MPS1/TTK. In this study, we identified a number of genes known to regulate aneuploidy and mitosis, and subsequently focused on *PRR14L*, a ubiquitously expressed gene previously implicated in chronic myelomonocytic leukemia (CMML). Proximity labeling of PRR14L using TurboID revealed several cell division proteins, including the PP2A-B56 phosphatase complex and the spindle assembly factor TACC3, as PRR14L-interacting proteins. Loss of PRR14L prolongs SAC-dependent mitotic arrest in response to microtubule depolymerization but, paradoxically, leads to catastrophic mitotic errors upon SAC abrogation by MPS1 inhibitors. A model derived from our findings provides a rationale for exploiting MPS1 inhibition as a potential vulnerability in cancers containing either PRR14L loss of function mutations or FGFR-TACC3 fusions.

Significance Statement

- Aneuploidy is a hallmark of cancer. Whether aneuploidy can be selectively targeted is not known.
- Utilizing a CRISPR/Cas9 screen, the authors found that loss of the gene PRR14L sensitizes cells to aneuploidy induction. Taking advantage of live cell imaging and proximity labeling, they linked PRR14L to TACC3 and mitosis.
- These findings suggest that spindle checkpoint inhibitors may have therapeutic potential in cancers with either loss-of-function PRR14L and/or gain of function TACC3 mutations.

Introduction

Intratumor heterogeneity, drug resistance, and metastasis constitute major challenges in cancer therapy. All these have been associated with aneuploidy, a cellular state whereby the chromosome number is not a multiple of the haploid set. Aneuploidy in cancer is a consequence of chromosomal instability (CIN) due to heightened frequency of chromosome mis-segregation (Bakhoum and Landau, 2017; Bakhoum *et al.*, 2018; Replogle *et al.*, 2020). Common mechanisms that drive CIN in tumors include merotelic attachments, increased centrosome copy number, and whole genome duplication (Thompson and Compton, 2008; Gordon et al., 2012; Baker et al., 2024), but the molecular defects which underpin these mitotic errors remains incompletely understood. The spindle assembly checkpoint (SAC) is a key safeguard that prevents mitotic errors by delaying mitosis in the presence of improper kinetochore-microtubule attachments and other mitotic defects. Although mutations in SAC genes enhance tumorigenesis in animal models, SAC mutations are surprisingly rare in human tumors (Dobles *et al.*, 2000; Baker *et al.*, 2004; Schvartzman *et al.*, 2010).

60 In this study, we performed a genome-wide CRISPR/Cas9 knockout (KO) screen in that
61 aimed to identify genes and pathways that affect the frequency of or influence the cellular
62 response to chromosomal mis-segregation. The screen was conducted with the MPS1/TTK
63 inhibitor NMS-P715, and was designed to uncover genes whose loss either sensitized cells to
64 SAC abrogation or modified the fitness of aneuploid progeny. Our screen identified *PRR14L,* a
65 poorly understood nuclear gene which has loss of function mutations associated with clonality in
66 chronic myelomonocytic leukemia (CMML) (Chase *et al.*, 2019). In order to further characterize
67 the function of *PRR14L*, we took advantage of proximity labeling with Turbo-ID to identify putative
68 interacting proteins. The proximal proteome suggested that PRR14L may regulate mitosis, which
69 we explored with live cell imaging in tandem with a variety of anti-mitotic treatments. Based on
70 the putative link discovered between PRR14L and TACC3, we propose that MPS1/TTK inhibitors,
71 such as NMS-P715, may have potentially unharnessed value as adjuvant treatments in tumors
72 with either PRR14L loss of function and/or TACC3 gain of function mutations.

73

Results and Discussion

A CRISPR/Cas9 screen to identify enhancers and suppressors of MPS1i

To identify genes that may regulate aneuploidy induction and/or survival, we performed a genome-wide CRISPR/Cas9 KO screen utilizing a previously established NALM-6 pre-B cell lymphoblastic leukemia line, with a doxycycline-inducible Cas9, and the extended-knockout (EKO) sgRNA library harboring 278,754 sgRNAs (Bertomeu *et al.*, 2018). Cells were treated for 7 days with doxycycline to induce Cas9 mediated gene KO, followed by a 2 day treatment with either 1 μM NMS-P715, to inhibit MPS1/TTK and induce aneuploidy, or vehicle control. NMS-P715 was subsequently washed out and cells were allowed to recover for 6 days in drug free media prior to analysis (Narkar *et al.*, 2021). We then compared the frequency of sgRNAs between DMSO control and the NMS-P715 treated population to identify genes which may enhance or suppress the effect of MPS1/TTK inhibition (**Fig. 1A and B**).

Analysis of enriched sgRNAs revealed a number of genes that either encode anaphase-promoting complex (APC/C) subunits or regulate APC/C activity. This finding corroborates previous reports showing that a reduction in APC/C activity, which delays mitotic exit, can compensate for a disrupted SAC to limit chromosomal instability (**Fig. 1C**) (Sansregret *et al.*, 2017). Another subset of suppressor genes encoded protein phosphatase 2A (PP2A) subunits or their regulators, consistent with the idea that loss of PP2A mitigates SAC silencing (Lara-Gonzalez *et al.*, 2021).

The depleted sgRNAs identified by our screen affected a more diverse profile of genes (**Fig. 1d**). We identified a number of essential genes (*e.g. DDX3X and NCAPH2*),

97 some of which also have well-established roles in mitosis (*e.g. BUB1B* and *ZWINT*). We
98 decided to focus further investigation on *PRR14L*, a poorly understood gene
99 hypothesized to play a role in cell division. *PRR14L* encodes a 237 kDa protein
100 previously linked to myeloid neoplasms, PP2A, and PLK1 activity (Chase *et al.*, 2019,
101 2023; Normandin *et al.*, 2023).

102

103 **Proximity labeling to identify likely interacting proteins of PRR14L.**

104 To gain insight into the cellular function of *PRR14L*, we used TurboID (Branon *et*
105 *al.*, 2018; Cho *et al.*, 2020) to identify the proximal proteome of PRR14L. HCT116 cells
106 were generated which stably expressed PRR14L fused to 3xHA-TurboID via a glycine-
107 serine linker (referred to as PRR14L-GS-3xHA-TurboID) and a spatial control for
108 nuclear localization (3xHA-TurboID-3xNLS). We first validated nuclear localization of
109 these construct with anti-HA antibodies and biotin labeling. In the spatial control cells
110 with 3xHA-TurboID-3xNLS, we observed nuclear localization of the construct and strong
111 labeling of the nucleoli. In contrast, PRR14L-GS-3xHA-TurboID localized primarily to the
112 nucleoplasm and displayed weak biotin labeling of the nucleoplasm and nucleoli (**Fig.**
113 **2B**). To confirm that 3xHA-TurboID-3xNLS and PRR14L-GS-3xHA-TurboID labeled
114 different proximal proteins, we generated cell lysates from untransfected, unlabeled and
115 labeled cells and probed for both the HA-tag and biotinylated proteins (**Fig. 2C**).
116 Western blot analysis revealed notably different biotin-labeling patterns between the two
117 constructs, with strong PRR14L self-labeling and weaker labeling of other proteins.

118 For mass spectrometry analysis, we proceeded with a 4-sample experiment
119 design using a tandem mass tag (TMT) approach (**Fig. 2A**) (Branon *et al.*, 2018). To
120 control for endogenously biotinylated proteins and non-specific binding to the
121 streptavidin beads, we included a no ligase control labeled with 134N. To account for
122 background labeling of nuclear proteins, we included the spatial control, 3xHA-TurboID-
123 NLS, labeled with 133C. Two independent experiments using PRR14L-GS-3xHA-
124 TurboID, were labeled with 133N and 126C respectively (see Materials and Methods for
125 further details).

126 We observed a linear correlation between labeling of the spatial control and both
127 PRR14L independent experiments as expected (**Sup. Fig. 1A and B**). Importantly, the
128 two independent experiments had a strong linear correlation with a R^2 of 0.899 (**Sup.
129 Fig. 1C**). We utilized ER membrane and cell membrane proteins as false positive filters
130 (**Sup. Fig. 1D-G,** see methods). The two sets of filters reduced the potential PRR14L
131 proximal proteome roughly 50-fold (**Sup. Fig. 1H and I**). Overlapping of the two
132 independent experiments yielded the final PRR14L proximal proteome list, where
133 PRR14L itself was the most enriched as expected (**Sup. Fig. 1J**). GO annotation
134 identified several categories of proteins, including protein quality control, nuclear import,
135 and mitochondria (**Sup. Fig. 1K-N**). A subset of proteins found were related to cell
136 division and dephosphorylation (**Fig. 2D, Sup. Fig. 1K**). PRR14L has a C-terminal
137 tantalus domain that is suggested to bind B56-family regulatory subunit of PP2A, and
138 two of these subunits were identified within our Turbo-ID experiment (Serine/threonine-
139 protein phosphatase 2A 56 kDa regulatory subunit alpha and delta isoforms). PRR14L
140 proximity labeling also identified TACC3, which was validated via western blot (**Fig. 2E**).

141 TACC3 is a centrosome and spindle protein that is a substrate of AURKA and thus
142 hypothesized to be regulated by PP2A, as well as a known oncoprotein (Still *et al.*,
143 1999; Lin *et al.*, 2010; Wong *et al.*, 2025).

144

145 ***Loss of PRR14L alters the response of cells to anti-mitotic drugs***

146 To study the cellular function of PRR14L, we generated *PRR14L* knockouts
147 (*PRR14L*$^{-/-}$) in the near diploid HCT116 human colon carcinoma cell line. We chose this
148 cell line because it is chromosomally stable and also adherent, allowing us to more
149 easily visualize mitosis. The success of CRISPR knockout was validated via both
150 genotyping and qPCR quantification of mRNA expression (**Sup. Fig. 2A and B**).
151 Protein-level validation was not successful using commercially available antibodies for
152 PRR14L, due to the presence of off-target antigens and likely also low endogenous
153 expression of the protein (data not shown). As a non-targeting control (*NTC*), we
154 generated monoclonal HCT116 cells transduced with LentiCRISPR v2 carrying a
155 protospacer not predicted to be in the human genome.

156 Given the nuclear localization of PRR14L (Chase *et al.*, 2019), we investigated
157 whether *PRR14L*$^{-/-}$ caused a global change in gene transcription by bulk RNA-
158 sequencing comparing *PRR14L*$^{-/-}$ cells with *NTC* cells. This revealed 375 differentially
159 expressed genes and GO analysis suggested an effect on cell differentiation
160 (Supplementary Tables 1,2). GSEA analysis revealed activation of interferon alpha
161 response and epithelial mesenchymal transition signatures, as well as suppression of
162 the G2/M checkpoint when comparing loss of PRR14L to control (**Sup Fig. 2C).** Further

163 analysis with PROGENy revealed significant upregulation of the WNT pathway in
164 PRR14L knockouts (**Sup Fig. 2D)**. However, the data does not suggest a general role
165 for PRR14L in transcriptional regulation, and the differential gene expression that we
166 observed could be attributable either to loss of PRR14L or cellular adaptation.

167 The proximity between PRR14L and both PP2A-B56 regulatory subunits and a
168 putative PP2A substrate led us to hypothesize that PRR14L plays a role in regulating
169 mitosis. To test this, we generated HCT116 *NTC* and HCT116 *PRR14L*$^{-/-}$ cells
170 expressing both H2B-mNeonGreen to label chromatin, and mCherry-CAAX to label the
171 cell membrane. Surprisingly, live cell imaging revealed no significant difference in NEBD
172 to anaphase time between control and *PRR14L*$^{-/-}$ cells (**Fig. 3A**). Additionally,
173 metaphase chromosome spreads revealed no significant difference in chromosome
174 numbers between the control and *PRR14L*$^{-/-}$ cells (**Supplementary Fig. 3A**). These
175 results suggested that under unperturbed conditions, *PRR14L*$^{-/-}$ cells undergo what
176 appear to be normal mitoses.

177 Since PP2A-B56 is known to play a role in SAC silencing (Vallardi *et al.*, 2019),
178 we next tested the strength of the SAC in *PRR14L*$^{-/-}$ cells by treating cells with low dose
179 (25 nM) nocodazole and observing the duration of mitosis. Notably, *PRR14L*$^{-/-}$ cells
180 spent a significantly longer time in mitosis than the control in the presence of low dose
181 nocodazole (**Fig. 3B**). This suggests that either PRR14L contributes to SAC silencing,
182 and/or loss of PRR14L leads to mitotic defects that sensitize cells to nocodazole
183 treatment. If the loss of PRR14L strengthened the SAC, then we would expect that
184 *PRR14L*$^{-/-}$ cells should resist MPS1/TTK inhibition which weakens the SAC. However,
185 *PRR14L*$^{-/-}$ cells were found to have more prominent mitotic defects than control cells in

186 the presence of NMS-P715 that frequently resulted in highly asymmetric chromatin
187 distribution, with the most extreme case similar to monopolar division resulting in a
188 single daughter cell with DNA inheritance (**Fig. 3C and D**). In line with this observation,
189 metaphase chromosome spreads revealed that the ploidy of *PRR14L*$^{-/-}$ cells became
190 near-tetraploid after NMS-P715 treatment (**Sup. Fig. 3B**).

191 It is possible that *PRR14L*$^{-/-}$ cells only show mitotic defects when the SAC is
192 disrupted by MPS1i (Colombo et al., 2010). We thus observed the response of PRR14L^{-}
193 $^{/-}$ cells to ZM447439, an aurora kinase (AURK) inhibitor that disables SAC through an
194 alternative mechanism. Surprisingly, we found that although control cells often fail cell
195 division even with low-dose ZM447439 treatment, this cell division defect is partially
196 suppressed by *PRR14L*$^{-/-}$ (**Fig. 3C, Sup. Fig. 3D**). Thus, loss of PRR14L appears to
197 sensitize cells specifically to MPS1 inhibition and in fact compensates for AURK
198 inhibition.

199

200 ***Mutations affecting the PP2A- PRR14L-TACC3 axis sensitize cells to MPS1i***

201 Given that PRR14L loss of function mutations have been found in CMML and are
202 potentially sufficient for clonality, we asked whether MPS1i can be used to eliminate
203 PRR14L deficient cells using a competition assay. HCT116-NTC cells were stably
204 transfected with mNeonGreen and HCT116-*PRR14L*$^{-/-}$ with mScarlet. These cells were
205 initially mixed with equal proportion and their relative abundance were tracked over 9
206 days in either DMSO or 1 μM NMS-P715 (**Fig. 4A and B**). *PRR14L*$^{-/-}$ cells were
207 significantly more sensitive to MPS1i relative to control (**Fig. 4C**), and this finding also

208 holds for both reversine and AZ-3146, other well-established MPS1/TTKi (**Sup. Fig. 3D**)
209 (Hewitt *et al.*, 2010; Santaguida *et al.*, 2010).

210 Based on findings described above, we propose a preliminary model whereby
211 PRR14L serves as an adaptor protein that facilitates phosphatase access to a subset of
212 its substrates (**Fig. 4D)**. This model posits that PRR14L acts as a scaffold bringing
213 PP2A-B56 into proximity with TACC3, whose function is regulated by a phosphorylation
214 balance between Aurora A kinase and PP2A. If true, this would suggest that loss of
215 PRR14L could potentially phenocopy TACC3 overactivation due to FGFR-TACC3 gene
216 fusions - driver mutations in cervical cancer, glioblastoma, and NSCLC (Singh *et al.*,
217 2012; Capelletti *et al.*, 2014; Carneiro *et al.*, 2015). Both genetic alterations - loss of the
218 PRR14L scaffold or FGFR-TACC3 fusion - may converge on TACC3 dysregulation,
219 creating a synthetic lethal vulnerability to MPS1 inhibition. Supporting this idea, analysis
220 of data from the Cancer Dependency Map portal (DepMap) revealed that the three
221 cancer cell lines that harbor a FGFR-TACC3 fusion are sensitive to both NMS-P715 and
222 reversine (**Fig. 4E**).

223 In summary, findings of this study provide further insight into the role of PRR14L
224 as a regulator of mitotic fidelity whose function is particularly prominent when MPS1 is
225 inhibited. We hypothesize that PRR14L functions as a scaffold for the PP2A-B56
226 phosphatase, coordinating the dephosphorylation of distinct substrates to ensure proper
227 chromosome segregation. The paradoxical sensitivity to MPS1 and resistance to aurora
228 kinase inhibition suggests a dual role for PRR14L. On one hand, its loss impairs PP2A-
229 B56 mediated SAC silencing, leading to prolonged arrest in nocodazole. On the other
230 hand, PRR14L appears critical for maintaining spindle integrity, likely via TACC3

231 regulation. When MPS1 is inhibited, the SAC is bypassed, and this underlying spindle
232 fragility leads to catastrophic errors, overwhelming the cell despite the potentially
233 hyperactive SAC machinery. Our results point to a potential vulnerability toward MPS1
234 inhibitors with driver mutations impact the PP2A- PRR14L-TACC3 axis and suggest a
235 testable therapeutic strategy for such genetically defined cancers.

236

237 **Materials and Methods**

REAGENT or RESOURCE	SOURCE	IDENTIFIER
Antibodies		
Mouse monoclonal anti-alpha Tubulin [DM1A]	Cell Signaling Technology	Cat#3873S; RRID:AB_1904178
Rabbit polyclonal anti-CEP152	Abcam	Cat# ab183911; RRID:AB_3106957
Rabbit monoclonal anti-TACC3 [EPR7756]	Abcam	Cat# ab134154; RRID: AB_3492052
Mouse monoclonal anti-gamma Tubulin [GTU-88]	Sigma-Aldrich	Cat#T6557; RRID:AB_477584
Rabbit polyclonal anti-PRR14L	Atlas Antibodies	Cat#HPA062645; RRID:AB_2684817
Rabbit polyclonal anti-C22ORF30	Origene	Cat#TA331394; RRID: AB_3492053
Rabbit monoclonal anti-HA-tag	Cell Signaling Technology	Cat#3724S; RRID: AB_1549585
Goat anti-Rabbit IgG (Heavy chain), Superclonal Recombinant Secondary Antibody, Alexa Fluor 488	Invitrogen	Cat#A27034; RRID:AB_2536097
Goat anti-Mouse IgG (H+L), Superclonal Recombinant Secondary Antibody, Alexa Fluor 488	Invitrogen	Cat#A28175; RRID:AB_2536161
Goat anti-Rabbit IgG (H+L) Cross-Adsorbed Secondary Antibody, Alexa Fluor 568	Invitrogen	Cat#A-11011; RRID:AB_143157
Goat anti-Mouse IgG (H+L) Cross-Adsorbed Secondary Antibody, Alexa Fluor 568	Invitrogen	Cat#A-11004; RRID:AB_2534072
Goat anti-Rabbit IgG (Heavy chain), Superclonal Recombinant Secondary Antibody, Alexa Fluor 647	Invitrogen	Cat#A27040; RRID: AB_2536101
Goat anti-Mouse IgG (H+L), Superclonal Recombinant Secondary Antibody, Alexa Fluor 647	Invitrogen	Cat#A55060; RRID: AB_2921068
IRDye 680RD Goat anti-Rabbit IgG Secondary Antibody	LICORbio	Cat#926-68071; RRID: AB_10956166
IRDye 680RD Goat anti-Mouse IgG Secondary Antibody	LICORbio	Cat#926-68070; RRID:AB_10956588
IRDye 800CW Goat anti-Rabbit IgG Secondary Antibody	LICORbio	Cat#926-32211; RRID:AB_621843
IRDye 800CW Goat anti-Mouse IgG Secondary Antibody	LICORbio	Cat#926-32210; RRID:AB_621842
Chemicals, peptides, and recombinant proteins		
NMS-P715	Calbiochem	475949; CAS: 1202055-32-0
Reversine	Selleckchem	S7588; CAS: 656820-32-5
AZ-3146	Selleckchem	S2731; CAS: 1124329-14-1
ZM 447439	Selleckchem	S1103; CAS: 331771-20-1
PMSF Protease Inhibitor	Thermo Scientific	36978; CAS: 329-98-6
Pierce Universal Nuclease for Cell Lysis	Thermo Scientific	88700
Alisertib (MLN8237)	Selleckchem	S1133; CAS: 1028486-01-2

Nocodazole	Sigma-Aldrich	SML1665; CAS: 31430-18-9
Paclitaxel	Sigma-Aldrich	T7191; CAS: 33069-62-4
Doxycycline hyclate	Sigma-Aldrich	D5207; CAS: 24390-14-5
Hoechst 33342 trihydrochloride	Santa Cruz Biotechnology	200908; CAS: 23491-52-3
Alt-R S.p. Cas9 Nuclease V3	IDT	1081059
Critical commercial assays		
DNEasy Blood & Tissue Kit	Qiagen	69504
SE Cell Line 96-well Nucleofector Kit	Lonza	V4SC-1096
PureLink Genomic DNA Mini Kit	Invitrogen	K182001
PureLink DNAse Set	Invitrogen	12185010
High-Capacity cDNA Reverse Transcription Kit	Applied Biosystems	4368814
PerfeCTa SYBR Green SuperMix	Quantabio	95054
SiR-Tubulin Kit	Cytoskeleton, Inc.	CY-SC002
QIAquick Gel Extraction Kit	QIAGEN	28704
NEBuilder HiFi DNA Assembly Master Mix	New England Biolabs	E2621
NucleoSpin Plasmid Transfection-grade, Mini kit for ultrapure plasmid DNA	MACHEREY-NAGEL	740490
Plasmid Plus Midi Kit	QIAGEN	12943
Lipofectamine 3000 Transfection Reagent	Invitrogen	L3000001
Pierce BCA Protein Assay Kits	Thermo Scientific	23225
PureLink RNA Mini Kit	Invitrogen	12183018A
Deposited data		
Raw mass spectrometry data	ProteomeXchange Consortium via the PRIDE partner repository	PXDXXXXXX
RNA-sequencing data	GEO	GSEXXXXXX
Experimental models: Cell lines		
NALM-6	Laboratory of Mike Tyers	
NALM-6 pCW-Cas9	Laboratory of Mike Tyers(Bertomeu *et al.*, 2018)	
NALM-6 PRR14L$^{-/-}$ Clone 5-3 (monoclonal)	This study	
NALM-6 PRR14L$^{-/-}$ Clone 6-8 (monoclonal)	This study	
HCT116	Laboratory of Bert Vogelstein	CCL-247
HCT116 NTC (monoclonal)	This study	
HCT116 NTC mNeonGreen (polyclonal)	This study	
HCT116 NTC H2B-mNeonGreen mCherry-CAAX (polyclonal)		
HCT116 PRR14L$^{-/-}$ Clone A3 (monoclonal)	This study	
HCT116 PRR14L$^{-/-}$ Clone A3 mScarlet (polyclonal)	This study	

HCT116 PRR14L$^{-/-}$ Clone A3 H2B-mNeonGreen mCherry-CAAX (polyclonal)	This study	
HCT116 PIKFYVE$^{-/-}$ Clone C2 (monoclonal)	This study	
HCT116 PIFKYVE$^{-/-}$ Clone C2 mScarlet (polyclonal)	This study	
HCT116 mNeonGreen (polyclonal)	This study	
HCT116 H2B-mNeonGreen mCherry-CAAX (polyclonal)	This study	
HCT116 H2B-mCherry (polyclonal)	This study	
HCT116 PRR14L$^{-/-}$ Clone 6-7 (monoclonal)	This study	
HCT116 PRR14L$^{-/-}$ Clone 6-7 mScarlet (polyclonal)	This study	
HCT116 PRR14L$^{-/-}$ Clone 6-7 H2B-mNeonGreen mCherry-CAAX (polyclonal)	This study	
HCT116 PRR14L$^{-/-}$ Clone 6-7 H2B-mCherry (polyclonal)	This study	
HCT116 PRR14L$^{-/-}$ Clone 6-10 (monoclonal)	This study	
HCT116 PRR14L$^{-/-}$ Clone 6-10 mScarlet (polyclonal)	This study	
HCT116 PRR14L$^{-/-}$ Clone 6-10 H2B-mNeonGreen mCherry-CAAX (polyclonal)	This study	
HCT116 PRR14L$^{-/-}$ Clone 6-10 H2B-mCherry (polyclonal)	This study	
hTERT RPE-1	Laboratory of Siew Cheng Phua	CRL-4000
hTERT RPE-1 TetON-PRR14L-TurboID (polyclonal)	This study	
hTERT RPE-1 PRR14L$^{-/-}$ Clone 5-9 (monoclonal)	This study	
hTERT RPE-1 PRR14L$^{-/-}$ Clone 5-9 TetON-PRR14L-TurboID (polyclonal)	This study	
hTERT RPE-1 PRR14L$^{-/-}$ Clone 5-22 (monoclonal)	This study	
293T	ATCC	CRL-3216
LentiX293T	Takara Bio	632180
HEK293FT	Invitrogen	R70007
Oligonucleotides		
Alt-R CRISPR-Cas9 crRNA targeting PRR14L (Azl_crR_005): TCCACTAGCCCACATCGCCC	IDT	
Alt-R CRISPR-Cas9 crRNA targeting PRR14L (Azl_crR_006): CTGTACCACGGCAGACATGG	IDT	
Alt-R CRISPR-Cas9 tracrRNA, ATTO 550	IDT	1075928
ON-TARGETplus Non-targeting Pool	Horizon Discovery	D-001810-10-05
On-TARGETplus Human PPP2CA (5515) siRNA – SMARTpool	Horizon Discovery	L-003598-01-0005
ACTB qPCR Primer (Fwd): GGATCAGCAAGCAGGAGTATG	IDT	
ACTB qPCR Primer (Rev): AGAAAGGGTGTAACGCAACTAA	IDT	
PRR14L qPCR Primer (Fwd): GCTACAAGCGCCTCAGATATAA	IDT	
PRR14L qPCR Primer (Rev): CCATCCACTAGCTGCCAAATA	IDT	
Recombinant DNA		
pBOB-EF1-FastFUCCI-Puro	Koh et al.(Koh *et al.*, 2017)	Addgene #86849
pBOB-EF1-Neon-Puro	This study	
pBOB-EF1-mScarlet-Puro	This study	

pMD2.G	Gift from Didier Trono	Addgene #12259
pRSV-Rev	Gift from Didier Trono	Addgene #12253
pMDLg/pRRE	Gift from Didier Trono	Addgene #12251
pLV-H2B-Neon-T2A-mCherry-CAAX	Johnson et al.(Johnson *et al.*, 2024)	
pBrain-GFP-TACC3KDP-shTACC3	Booth et al.(Booth *et al.*, 2011)	Addgene #59356
3xHA-TurboID-NLS_pCDNA3	Branon et al.(Branon *et al.*, 2018)	Addgene #107171
pPB-cT3G-cERP2-NR5A1	Smela et al.(Smela *et al.*, 2023)	Addgene #192915
pDonor-tBFP-NLS-Neo (Universal)	Katoh et al.(Katoh *et al.*, 2017)	Addgene #80767
pDonor-PRR14L-GS-3xHA-TurboID-BSD	This study	
pPB-cT3G-CERP2(BSD)-PRR14L-GS-3xHA-TurboID	This study	
pPRR14L-GS-Neon-FLAG	This study	
pPRR14L(1-1487)-GS-Neon-FLAG	This study	
pPRR14L(1488-2151)-GS-Neon-FLAG	This study	
pLenti6-H2B-mCherry	Pemble et al.(Pemble *et al.*, 2017)	Addgene #89766
Lenti-Centrin1-GFP	Gift from Alexey Khodjakov	
pRSETB/mStayGold	Ando et al.(Ando *et al.*, 2024)	Addgene #212017
lentiCRISPR v2	Sanajana et al.(Sanjana *et al.*, 2014)	Addgene #52961
lentiCRISPR v2-NTC	This study	
lentiCRISPR v2-PRR14L	This study	
lentiCRISPR v2-PIKFYVE	This study	
psPAX2	Gift from Didier Trono	Addgene #12260
Software and algorithms		
Fiji	Schneider et al.(Schneider *et al.*, 2012)	https://imagej.net/software/fiji/
R, version 4.4.0	R Core Team (2024)	https://www.R-project.org/
RStudio, version 2024.04.1	RStudio Team (2024)	
ICE CRISPR Analysis Tool	Conant et al.(Conant *et al.*, 2022)	
FlowJo	FlowJo LLC	https://www.flowjo.com/
Zen Blue, version 3.5	Zeiss	
ggplot2, version 3.5.1	Wickham et al.(Wickham, 2016)	
Other		
Puromycin Dihydrochloride	Gibco	A1113803
Blasticidin S HCl (10 mg/mL)	Gibco	A1113903
RPMI 1640 Medium	Gibco	11875093
Fetal Bovine Serum, Value, heat inactivated, OneShot format	Gibco	A5209501

Fetal Bovine Serum, Tet system approved, USDA-approved regions, OneShot format	Gibco	A4736301
Penicillin-Streptomycin (10,000 U/mL)	Gibco	15140122
DMEM, high gluose	Gibco	11965092
DMEM/F-12	Gibco	11320033
Hygromycin B (50 mg/mL)	Gibco	10687010
GlutaMAX Supplement	Gibco	35050061
MEM Non-Essential Amino Acids Solution (100x)	Gibco	11140050
Lenti-X Concentrator	Takara	631232
Sodium Pyruvate (100 mM)	Gibco	11360070
Nunc Lab-Tek Chambered Coverglass	Thermo Scientific	155411
FluoroBrite DMEM	Gibco	A1896701
µ-slide 8 well	ibidi	80826
µ-slide 8 well high Glass Bottom	ibidi	80807
Glass Base Dish 27 mm	iwaki	3970-035
KaryoMAX Colcemid Solution in PBS	Gibco	15212012
Q5 High-Fidelity DNA Polymerase	New England Biolabs	M0491
Platinum SuperFi II Green PCR Master Mix	Invitrogen	12369010
NEB 5-alpha Competent E. coli (High Efficiency)	New England Biolabs	C2987
NEB Stable Competent E. coli (High Efficiency)	New England Biolabs	C3040
ProLong Gold Antifade Mountant	Invitrogen	P36930
Fibronectin (pure)	Roche	11051407001
D-Biotin	Invitrogen	B20656
RIPA Lysis and Extraction Buffer	Thermo Scientific	89900
Protease/Phosphatase Inhibitor Cocktail (100X)	Cell Signaling Technology	5872
Laemmli SDS sample buffer, reducing (6x)	Alfa Aesar	J61337
Precision Plus Protein Dual Color Standards	BIORAD	1610374
Spectra Multicolor High Range Protein Ladder	Thermo Scientific	26625
4-20% Mini-PROTEAN TGX Precast Protein Gels, 10-well, 50 µL	BIORAD	4561094
4-20% Mini-PROTEAN TGX Precast Protein Gels, 15-well, 15 µL	BIORAD	4561096
Trans-Blot Turbo Mini 0.2 µm Nitrocellulose Transfer Packs	BIORAD	1704158
Streptavidin, Alexa Fluor 488 conjugate	Invitrogen	S11223
Streptavidin Protein, DyLight 680	Invitrogen	21848
Opti-MEM I Reduced Serum Media	Gibco	31985070

238

239 **Cell culture**

240 NALM-6 cells were grown at 37 ˚C with 5% CO_2 in RPMI 1640 supplemented with 10%
241 heat-inactivated (HI) fetal bovine serum (FBS) and 100 U/mL Penicillin/Streptomycin
242 (Pen/Strep). HCT116 cells were grown at 37 ˚C with 5% CO_2 in DMEM supplemented

243 with 10% HI FBS and 100 U/mL Pen/Strep. hTERT RPE-1 cells were grown at 37 ˚C
244 with 5% CO_2 in DMEM/F12 supplemented with 10% HI FBS and 10 µg/mL Hygromycin
245 B. 293T cells were grown at 37 ˚C with 5% CO_2 in DMEM supplemented with 10% HI
246 FBS, 100 U/mL Pen/Strep, and 1% GlutaMAX. HEK293FT cells were grown at 37 ˚C
247 with 5% CO_2 in DMEM supplemented with 10% HI FBS. LentiX293T cells were grown at
248 37 ˚C with 5% CO_2 in DMEM supplemented with 10% HI FBS, 1% GlutaMAX, 1x MEM
249 non-essential amino acids, 1 mM Sodium Pyruvate, and 50 U/mL Pen/Strep.
250 Mycoplasma testing was completed every 3-6 months to ensure cultures were free of
251 mycoplasma contamination.

252 **Genome-wide pooled CRISPR/Cas9 Screen**

253 The genome-wide pooled CRISPR/Cas9 screen was completed as previously
254 described(Bertomeu *et al.*, 2018; Normandin *et al.*, 2023). In brief, a custom sgRNA
255 library was used comprised of 233,268 sgRNAs that target 19,084 protein coding genes
256 and 17,139 alternatively spliced exons. Each gene was targeted by approximately 10
257 sgRNAs. Noise was controlled for via 2,043 non-targeting sgRNAs. A doxycycline-
258 inducible Cas9 clone of NALM-6 was used. The two conditions that were compared
259 were vehicle control (DMSO, 1:1000) and 1 µM NMS-P715. After doxycycline induction
260 for 1 week, DMSO and 1 µM NMS-P715 treatment were started Day 0 of the screen,
261 and washed out Day 2. Cells were collected on both Day 2 and Day 8 for gDNA
262 extraction and NGS.

263 **Generation of monoclonal KO cell lines**

264 Two independent methods were used to generate monoclonal KO cell lines.

265 Lentivirus method:

266 HCT116 PRR14L$^{-/-}$ clone A3 was generated using the lentiCRISPRv2 system. In
267 brief, lentiCRISPRv2-PRR14L was cloned using the protospacer 5'-
268 TCTGCTCTACCCTCTAATGG-3', and lentiCRISPRv2-PIKFYVE was cloned using the
269 protospacer 5'-ACATATGTTCGGTTAGCCTG-3'. Lentiviral particles were generated and
270 collected via Lipofectamine-based transient transfection of HEK293FT cells with the
271 following three plasmids in 1:1:1 molar ratio: lentiCRISPRv2, pMD2.G, and psPax2.
272 HCT116 cells were transduced with lentiviral particles at a MOI of 0.5-1, and then
273 underwent selection with 1 µg/mL Puromycin for 3 days followed by single cell sorting.
274 Genomic DNA (gDNA) was extracted from single cell clones using DNEasy Blood and
275 Tissue Kit (Qiagen) and amplified using the following primers: PRR14L: FWD 5'-
276 CTGTTGCTACCATCCCCAGA-3' | REV 5'-GAGACCACTTGAGGAAAGCCA-3'. PCR
277 product was purified and submitted for sanger sequencing using the primer: 5'-
278 CCACTTGAGGAAAGCCAGCT-3'. Sequencing data was analyzed using the ICE
279 analysis tool to assess for successful gene knockout via frameshift mutation(Conant *et*
280 *al.*, 2022). Control cells referred to as "HCT116 NTC" were generated in the exact same
281 manner except a non-targeting protospacer was used with the sequence 5'-
282 gccccgccgccctcccctcc-3'.

283 **Lentivirus Generation and Transduction**

284 Second generation lentivirus generation:

285 2 x 10^6 HEK293FT cells were seeded in a T-25 flask. After 24 hrs, cells were
286 transfected with the transfer plasmid, pMD2.G, and psPax2 in a 1:1:1 molar ratio using

287 Lipofectamine 3000. 48 hrs after transfection, lentivirus supernatant was collected,
288 aliquoted, and frozen at -80 ˚C for future use.

289 Third generation lentivirus generation:

290 Third generation lentivirus was produced following a previously published
291 protocol with a few modifications25. LentiX293T cells were used for lentivirus
292 production, and Lenti-X concentrator was used to concentrate lentiviral supernatants 5
293 to 10-fold. Concentrated lentiviral pellets were resuspended in DPBS and frozen at -
294 80 ˚C for future use.

295 Lentivirus transduction:

296 Lentivirus aliquots were warmed quickly using a 37 ˚C water bath for 2-3 min.
297 Cells were transduced with a mixture of fresh media, lentivirus supernatant, and 10
298 µg/mL polybrene for 48 hrs. This was followed by either antibiotic selection or
299 fluorescent-activated cell sorting (FACS) to obtain polyclonal and/or monoclonal cell
300 lines.

301 **Competition Assay**

302 Polyclonal fluorescent populations of competing cell lines were obtained by lentiviral
303 transduction of cell lines with pBOB-EF1-Neon-Puro or pBOB-EF1-mScarlet-Puro. Cells
304 were seeded at equal cell number on Day 0 in triplicate for each day to be measured,
305 *i.e.*, for a 9-day experiment with two different drug treatments, a total of 30 wells were
306 seeded initially. Media was changed to fresh media with drug treatment or control on
307 Day 1. Drug treatments were washed out on Day 3. Cells were passaged every 2 days
308 if the confluency was observed to be >75%; otherwise, a media change was completed.

309 Population numbers were measured using flow cytometry using either an Attune NxT
310 Flow Cytometer or a Sony SH800. Data were analyzed using FlowJo and plots were
311 generated with Rstudio and ggplot2.

312 **qPCR Profiling and Analysis**

313 RNA was extracted from cells using PureLink RNA Mini Kit in combination with
314 PureLink DNase Set. RNA concentration was measured with Nanodrop and then
315 normalized to 100 ng/μL with RNase free water. cDNA was generated using High
316 Capacity cDNA Reverse Transcriptase Kit. qPCR was completed using PerfeCTa SYBR
317 Green Supermix. Fold change was calculated using ddCt method with ACTB and/or
318 GAPDH as a control, and plots were generated with Rstudio and ggplot2.

319

320 **RNA Sequencing and Data Analysis**

321 Library Preparation and Sequencing Total RNA was extracted from HCT116 NTC and
322 PRR14L-/- (Clone A3) cells using the PureLink RNA Mini Kit (Invitrogen) with on-column
323 DNase treatment (PureLink DNase Set, Invitrogen), according to the manufacturer's
324 instructions. Stranded RNA sequencing library preparation and high-throughput
325 sequencing were performed by BGI Genomics (Hong Kong). Paired-end sequencing
326 (PE100) was conducted on the DNBSEQ platform.

327

328 Preprocessing and Quantification Raw FASTQ files were processed by BGI using their
329 internal analysis platform, Dr. Tom. Briefly, reads were quality-controlled, aligned to the

human reference genome (Ensembl release 105), and gene expression levels were quantified as raw read counts.

Differential Gene Expression (DGE) Analysis Differential gene expression analysis was performed in R (v4.4.0) using the DESeq2 package (Love et al., 2014). To improve visualization and ranking, log2 fold changes (LFC) were shrunk using the apeglm method (Zhu et al., 2019). Genes were considered significantly differentially expressed if they met the criteria of an FDR-adjusted p-value (padj) < 0.05 and an absolute LFC > 1 (2-fold change). Gene Set Enrichment Analysis (GSEA) GSEA was performed using the clusterProfiler package (Wu et al., 2021) against the MSigDB Hallmark gene sets, retrieved via msigdbr. Genes were ranked by the Wald statistic obtained directly from the DESeq2 results. Pathway activities were inferred using PROGENy (Schubert et al., 2018). VST-normalized expression data, aggregated to gene symbols, were used as input and pathway scores were calculated based on the expression of the top 100 footprint genes per pathway. Differential pathway activities between KO and NTC samples were determined by applying a robust Student's t-test to the inferred activity scores. Significance was determined by an FDR-adjusted p-value < 0.05.

Live Cell Imaging

Live cell imaging was done via two methods based on location of experiment.

1. Cells were seeded in Nunc Lab-Tek chambered cover glass 2 days prior to imaging. Prior to the beginning of imaging, media was changed to fresh

352 FluoroBrite DMEM supplemented with HI FBS and Pen/Strep, with or without
353 drug treatment. Imaging was completed on a Zeiss LSM 780 laser scanning
354 confocal microscope with an environmental chamber kept at 37 ˚C with 5% CO_2
355 using a 63x oil-immersion objective (NA 1.4). For most independent experiments,
356 4-6 positions per genotype were imaged at once, with a 3 min time interval, and a
357 15-20 slice Z-stack with 1 µm slices. Deviations from this are mentioned in figure
358 captions. Images were processed in ImageJ, with adjustments to color balance
359 and cropping of selected cells of interest. Judgment of mitotic errors and/or
360 mitotic outcome was done manually. Any fluorescence intensity quantification
361 was done on unprocessed images.

362 2. Cells were seeded in ibidi µ-slides 2 days prior to imaging. 12 hrs prior to the
363 start of imaging, media was changed to fresh FluoroBrite DMEM supplemented
364 with HI FBS and 1x GlutaMAX. If drug treatment(s) were used, they were added
365 2 hrs prior to imaging in fresh FluoroBrite DMEM supplemented with HI FBS, 1x
366 GlutaMax, and 50 nM SiR-Tubulin. Imaging was completed on one of three
367 microscopes: Zeiss LSM 980 laser scanning confocal microscope with
368 environmental chamber, 63x oil-immersion objective (NA 1.4), in either confocal
369 mode, CO-8Y mode, or SR mode; Oxford Instruments BC43 spinning disk
370 confocal microscope with environmental chamber, 60x oil-immersion objective
371 (NA 1.42), and deconvolution completed with Imaris software; Zeiss Lattice
372 Lightsheet 7 with environmental chamber, water-based objective (NA 1.0), and
373 deskewing, cover glass transformation, and deconvolution was completed using
374 Zen Blue software.

375 **Metaphase Spreads**

376 Cells were treated with 100 ng/mL of colcemid for 6 hrs and then collected. Cell pellets
377 were resuspended in PBS, and then incubated with pre-warmed 75 mM KCl for 10 min
378 to induce cell swelling. Swollen cells were fixed with a solution of 3:1 methanol:glacial
379 acetic acid overnight at 4 ˚C. Fixed cells were dropped onto pre-humidified glass slides,
380 and then slides were dried by warming them to 65 ˚C on a hot plate for 20 min. Slides
381 were mounted with ProLong Gold Antifade Mountant with DAPI followed by the addition
382 of a coverslip and overnight curing at room temperature. Imaging was completed on a
383 Nikon TiE-Eclipse epifluorescence microscope with 60x oil immersion objective.
384 Chromosome number was recorded manually for each metaphase spread using the cell
385 counter plugin in ImageJ.

386 **Plasmid cloning**

387 A list of all plasmids used in this study can be found in the Recombinant DNA section of
388 the materials list. All plasmid generation was completed via Gibson assembly (Gibson *et*
389 *al.*, 2009). Primers to generate new plasmids were designed using
390 https://nebuilder.neb.com/#!/. For assemblies of 2 or 3 fragments, primers were
391 designed with 20 bp overlaps. For assemblies of 4+ fragments, primers were designed
392 with >24 bp overlaps. For assemblies requiring the addition of small fragments (e.g. GS
393 linker, T2A sequence), small single-stranded oligonucleotide donors (ssODNs) were
394 used. PCRs were completed using either Q5 Polymerase or Platinum SuperFi
395 Polymerase. Products were run on 1% agarose gels, and then bands of the correct size
396 were extracted using QIAquick Gel Extraction Kit. Gibson assembly was performed
397 using NEBuilder HiFi DNA Assembly Master Mix, and products were transformed into

398 either NEB 5-alpha Competent E. coli or NEB Stable Competent E. coli. Multiple single
399 colonies were picked to inoculate miniprep cultures, and plasmid DNA was extracted
400 using NucleoSpin Plasmid Transfection-grade, Mini kit. Plasmids were submitted for
401 sanger sequencing to confirm assembly junctions. Confirmed plasmids were then re-
402 picked to inoculate midiprep cultures, and plasmid DNA was extracted using QIAGEN
403 Plasmid Plus Midi Kit. Midipreps were then submitted for sequencing of all functional
404 genetic components (i.e. promoter, transgene, etc.) before being used for cell
405 transfection.

406 **Transient Transfection**

407 Transient transfection was carried out using Lipofectamine 3000, following the
408 manufacturer's instructions with a few modifications. The amount of OptiMEM Reduced
409 Serum Media used was doubled, and prior to transfection the same amount of OptiMEM
410 to be added was removed from cell culture. Lipofectamine 3000:P3000 Reagent::1.18:1.
411 P3000 Reagent:Plasmid DNA::2 µL:1 µg. Cells were analyzed between 24-72 hrs after
412 transfection.

413 **TurboID Immunofluorescence Validation**

414 The following protocol is based on previously published work with slight
415 modifications(Cho *et al.*, 2020). Ibidi µ-slides 8-well were coated with 200 µL of 50
416 µg/mL fibronectin in DPBS per well for 30 min. $3.6x10^4$ 293T cells were seeded per well.
417 After 24 hours, TurboID constructs were transfected using Lipofectamine 3000. After
418 another 24 hours, media was replaced with fresh warm cDMEM supplemented with 50
419 µM biotin for either 10 min (3xHA-TurboID-3xNLS) or 20-30 min (PRR14L-GS-3xHA-

420 TurboID). Labeling was stopped with 5x ice cold DPBS washes followed by fixation with
421 4% PFA in PBS at RT for 10-15 min. Blocking and permeabilization was completed
422 simultaneously with 1 hr incubation with AbdIl (2% BSA, 0.1% Triton X-100, in TBS).
423 1˚ antibody against HA-tag was incubated overnight (O/N) at 4 ˚C diluted 1:1,200 in
424 AbdIl. Cells were washed 3x with TBST (0.1% Triton X-100 in TBS) followed by 1hr
425 room temperature (RT) incubation with 2˚ antibodies diluted in AbdIl: anti-rabbit
426 conjugated with Alexa Fluor 568 (1:1,000) and Streptavidin conjugated with Alexa Fluor
427 488 (1:1,000). Cells were washed 1x with TBST, followed by counterstaining with
428 Hoechst 33342 in TBST for 5 min RT, followed by 1x TBST rinse, 1x TBST wash, and
429 cells were imaged in 1x TBS buffer.

430 **Western Blot for TurboID Validation**

431 $3x10^5$ 293T cells were plated per well in 6-well plates. After 24 hours, TurboID
432 constructs were transfected using Lipofectamine 3000. After another 24 hours, media
433 was replaced with fresh warm cDMEM supplemented with 50 μM biotin for either 10 min
434 (3xHA-TurboID-3xNLS) or 20-30 min (PRR14L-GS-3xHA-TurboID). Labeling was
435 stopped with 5x ice cold DPBS washes followed by use of 1mL ice cold DPBS to detach
436 cells and collect cell pellets. Cell pellets were resuspended in 100 μL of RIPA buffer
437 supplemented with 1x protease and phosphatase inhibitor, 1 mM PMSF, and Pierce
438 universal nuclease for cell lysis, and lysed for 20-40 min on ice with thorough pipetting
439 every 10 min. Lysates were clarified by centrifugation at 14,000 rcf for 15 min at 4 ˚C. 80
440 μL of supernatant was collected and 5 μL was used for BCA protein quantification.
441 Protein concentration was normalized across samples and then combined with 6x
442 Laemmli sample buffer and boiled for 10 min. Samples were loaded onto Mini-

443 PROTEAN TGX precast protein gels, 4-20%, either 15x15 µL wells or 10x50 µL wells
444 with either Precision Plus Dual Protein Color Standards or Spectra Multicolor High
445 Range Protein Ladder for molecular weight ladder. Samples were transferred onto 0.2
446 µm nitrocellulose blots using the Trans-Blot Turbo transfer system, mixed molecular
447 weight protocol. Blots were blocked with Intercept (TBS) Blocking buffer for 1 hr at RT
448 followed by O/N incubation with 1˚ Ab (anti-HA). Blots were washed 4x with TBST (0.1%
449 Tween-20 in TBS) followed by 1 hr incubation with 2˚ Ab diluted in 1:1::blocking
450 buffer:TBST – Streptavidin Dylight 680 (1:5,000) and IRDye 800CW Goat anti-Rabbit
451 IgG Secondary Antibody (1:20,000). Blots were washed again with 4x TBST followed by
452 2x TBS, and then imaged on an Odyssey CLx Imager.

453 **TMT Mass Spectrometry**

454 2.25×10^6 293T cells were plated in T-75 flasks, two T-75 flasks per independent
455 experiment. After 24 hours, TurboID constructs were transfected using Lipofectamine
456 3000. After another 24 hours, media was replaced with fresh warm cDMEM
457 supplemented with 50 µM biotin for either 10 min (No ligase control and 3xHA-TurboID-
458 3xNLS) or 30 min (PRR14L-GS-3xHA-TurboID). Labeling time of the PRR14L construct
459 was extended to compensate for the weaker labeling by the PRR14L fusion construct
460 relative to control. Labeling was stopped with 5x ice cold DPBS washes followed by use
461 of 7.5 mL ice cold DPBS per flask to detach cells and collect cell pellets. Cell pellets
462 were resuspended in 1.5 mL of RIPA buffer supplemented with 1x protease and
463 phosphatase inhibitor, 1 mM PMSF, and Pierce universal nuclease for cell lysis, and
464 lysed for 50 min on ice with thorough pipetting every 10 min. Lysates were clarified by
465 centrifugation at 14,000 rcf for 15 min at 4 ˚C. Streptavidin magnetic beads were

466 washed twice with 1 mL RIPA. 15 µL of lysate was retained as input, and the remainder
467 was loaded on the streptavidin beads O/N rotating at 4 ˚C. 15 µL of flowthrough was
468 collected per sample, and then beads were washed with: 2x 1 mL RIPA (2 min per
469 wash), 1x 1mL KCl (2 min), 1x 1mL 100 nM Na_2CO_3 (10 sec), 1x 1mL 2M urea in 10 mM
470 Tris-HCl pH 8.0 (10 sec), 2x 1 mL RIPA (2x 2min). The beads were resuspended in 1mL
471 RIPA, transferred to fresh microcentrifuge tubes, and then flash frozen in liquid nitrogen
472 and stored at -80 ˚C until further processing.

473 For each sample 100 µg of protein was added to a 10 kDa ultrafiltration tube, and
474 volume was normalized across samples. Samples were centrifuged at 20 ˚C, 12,000 rcf
475 for 20 min. 100 µL of 0.5M TEAB was added to samples and then centrifuged at 20 ˚C
476 12,000 rcf for 20 min (3x). Samples were subjected to Trypsin digestion at 37 ˚C for 4
477 hours. Peptide solution was concentrated and desalted, and the collected peptide
478 fractions were freeze-dried. For peptide labeling, each tube of TMT (0.8 mg) was
479 dissolved in 41 µL acetonitrile and shaken for more than 1 min. Peptide fragments were
480 resuspended in 0.1M TEAB to a concentration of 3.74 µg/µL. 100 µg of peptide was
481 labeled with 41 µL of TMT reagent for 2 hr at room temperature, ensuring pH was
482 between 7-8.

483 For peptide fractionation the Shimadzu LC-20AB liquid phase system was used
484 with a 5 µm 4.6x250mm Gemini C18 column for liquid phase separation of the sample.
485 Dried peptide samples were reconstituted with mobile phase A (5% acetonitrile pH 9.8)
486 and injected, eluting at a flow rate of 1 mL/min with the following gradients: 5% mobile
487 phase B (95% acetonitrile, pH 9.8) for 10 min. 5% to 35% mobile phase B for 40 min.
488 35% to 95% mobile phase B for 1 min, mobile phase B for 3 min, and 5% mobile phase

489 B for 10 min. The elution peak was monitored at a wavelength of 214 nm and one
490 component was collected per minute, and the samples were combined according to the
491 chromatography elution peak map to obtain 20 fractions, which were then freeze-dried.

492 For HPLC the dried peptide samples were reconstituted with mobile phase A (2%
493 acetonitrile, 0.1% formic acid), centrifuged at 20,000 rcf for 10 min, and the supernatant
494 was used for injection. Separation was performed using a Easy-nLC 1200, followed by a
495 tandem self-packed C18 column (75 μm internal diameter, 1.9 μm column size, 25 cm
496 column length) and separated at a flow rate of 200 nL/min using the following gradient:
497 0 – 3 min, 5% mobile phase B (80% acetonitrile, 0.1% formic acid); 3 – 45 min, mobile
498 phase B was linearly increased from 8 to 44%; 45-50 min, mobile phase B increased
499 from 44 to 60%; 50-53 min, mobile phase B rose from 60 to 100%; 53-60 min, 80%
500 mobile phase B. The nanoliter liquid phase separation was directly connected to the
501 mass spectrometer.

502 For mass spectrometry detection, the peptides separated by HPLC were ionized
503 by a nanoESI source and then passed to a tandem mass spectrometer Orbitrap
504 Exploris 480 for DDA mode detection. Parameters included: ion source voltage = 1.9
505 kV; MS1 mass spectrometer scanning range was 350-1,600m/z; resolution was set to
506 60,000; MS2 starting m/z was fixed at 100; resolution was 15,000. The ion screening
507 conditions for MS2 fragmentation were: charge 2+ to 7+, and the first 30 parent ions
508 with peak intensity exceeding $2x10^4$. Ion fragmentation mode was HCD, and the
509 fragment ions were detected in Orbitrap. The dynamic exclusion time was set to 30
510 seconds. The automatic gain control was set to: MS1 300%, MS2 standard.

Mass spectrometry analysis was completed using Spectrum Mill MS Proteomics software as well as R.

To distinguish specific proximal proteins from abundant nuclear background, we employed a filtering strategy based on a custom False Positive Identification (FPI) rate, calculated against curated lists of proteins from irrelevant subcellular compartments (e.g., ER membrane, cell membrane) obtained from UniProt. This approach allowed us to apply stringent cutoffs to enrich for high-confidence interactors. A full list of identified proteins and quantitative values is provided in Supplementary Table 3. For the first filter where we compared abundance of proteins labeled by PRR14L relative to no ligase control, we applied a stringent cut-off of FPI < 0.03, given that we expect that almost all the proteins identified in our no ligase control should be non-specific, using a false positive list of ER membrane proteins. For the second filter where we compared abundance of proteins labeled PRR14L relative to the nuclear spatial control, a more relaxed cut-off of FPI < 0.05 was applied. This is because a greater percentage of labeling overlap is expected when both PRR14L and the spatial control occupy the nucleus. For this cut-off, we used a false positive list of cell membrane proteins.

Acknowledgments

A.Z.L., and B.A.J. received support from the NIH Medical Scientist Training Program T32GM136577. This work was supported by Bloomberg Professorship funds to R.L. from Johns Hopkins University, a Mid-sized Grant (NRF-MSG-2023-0001) from Singapore National Research Foundation to R.L. and a Canadian Institutes of Health Research grant (FDN-167277) to M.T. We thank Angela Xiong for assistance with molecular cloning. Portions of the text were edited with the assistance of ChatGPT (OpenAI), a large language model AI tool.

Declaration of Interests

The authors declare no competing interests.

Data and code availability

Mass spectrometry and RNA-sequencing data will be deposited in publicly accessible databases prior to official publication.

553 **Figure Titles and Legends**

554 **Figure 1.** NALM-6 genome-wide CRISPR/Cas9 screen identifies *PRR14L* as an
555 enhancer of NMS-P715

556 (A) Workflow of CRISPR/Cas9 screen
557 (B) (left) Rationale underlying observation of enhancer sgRNAs (center) Volcano plot
558 of CRISPR/Cas9 screen (right) Rationale underlying observation of suppressor
559 sgRNAs.
560 (C) Zoom-in on suppressor sgRNAs, with gene names highlighted, colored by gene
561 category.
562 (D) Zoom-in on enhancer sgRNAs, with gene names highlighted

563 **Figure 2.** TurboID proximity labeling of PRR14L identifies multiple cell division proteins

564 (A) Schematic of TurboID Tandem Mass Tag (TMT) mass spectrometry experiment
565 completed in HEK293T cells.
566 (B) Differences between TurboID-NLS and PRR14L-TurboID localization.
567 Representative images of hTERT RPE-1 cells transiently transfected with either
568 3xHA-TurboID-3xNLS or PRR14L-GS-3xHA-TurboID followed by 10 or 15 min
569 labeling with 50 μM biotin respectively. Images acquired on LSM980, SR-8Y
570 mode.
571 (C) Characterization of biotinylation by PRR14L-TurboID. HEK293T cells were
572 transiently transfected with either 3xHA-TurboID-3xNLS or PRR14L-GS-3xHA-
573 TurboID followed with or without incubation with 50 μM biotin for 20 min. Cell
574 lysates were used for western blot, and probed with anti-HA antibody and

575 Streptavidin Dylight 680. Untransfected (no ligase) control also included for
576 comparison.
577 (D) PRR14L proximal proteome includes cell division proteins regulated by PP2A.
578 Scatter plot of final PRR14L proximity proteome determined by mass
579 spectrometry with PRR14L itself excluded. Dots colored by GO annotation.
580 Proteins with GO annotations related to cell division have their names
581 highlighted.
582 (E) Western blot validation of PRR14L and TACC3 proximity. TurboID experiment
583 was repeated, and cell lysates were utilized for anti-TACC3 western blot.

584 **Figure 3.** Loss of *PRR14L* alters the response to anti-mitotic drugs

585 (A) Quantification of untreated mitotic duration. Beeswarm plot comparing NEBD to
586 anaphase time in HCT116 NTC and *PRR14L*$^{-/-}$ Clone A3 stably expressing H2B-
587 mNeonGreen and mCherry-CAAX measured via live cell imaging. Colors denote
588 independent experiments (n=3), small dots denote individual cells (NTC n = 48,
589 *PRR14L*$^{-/-}$ n = 48), large dots denote mean of independent experiment. p-value
590 calculated via Mann U-Whitney test using replicate averages, ns = non-
591 significant. Images acquired on Zeiss LSM 780.
592 (B) Quantification of mitotic duration in the presence of 25 nM nocodazole. Kaplan-
593 Meier curve of % of cells still remaining in mitosis in HCT116 *NTC* and *PRR14L*$^{-/-}$
594 Clone A3 stably expressing H2B-mNeonGreen and mCherry-CAAX measured
595 via live cell imaging. + marks denote censored events, where the cell still
596 remained in mitosis at the end of the movie. n = 3 independent experiments.
597 Total number of observed mitoses (NTC n = 51, PRR14L$^{-/-}$ n = 44). p-value

598 calculated via logrank test on combined data from independent experiments.
599 Images acquired on Zeiss LSM 780.

600 (C) Quantification of asymmetric chromosome partitioning in the presence of various
601 drug treatments. Combined beeswarm and bar plot comparing proportion of cells
602 undergoing asymmetric divisions between HCT116 *PRR14L*$^{+/+}$ and *PRR14L*$^{-/-}$
603 Clone A3 stably expressing H2B-mNeonGreen and mCherry-CAAX measured
604 via live cell imaging. Colors denote independent experiments (n=3), dots denote
605 mean of independent experiments with size correlated with number of mitoses
606 observed (For DMSO, *PRR14L*$^{+/+}$ n = 72, *PRR14L*$^{-/-}$ n = 77. For 1 μM NS-P715,
607 *PRR14L*$^{+/+}$ n = 68, *PRR14L*$^{-/-}$ n = 44. For 250 nM ZM447439 *PRR14L*$^{+/+}$ n = 68,
608 *PRR14L*$^{-/-}$ n = 55). p-value calculated using two-proportion Z-test using combined
609 data from independent experiments, ** = $p < 0.01$, **** = $p < 0.0001$. Images
610 acquired on Zeiss LSM 780.

611 (D) Representative images comparing live cell imaging of HCT116 *NTC* and
612 *PRR14L*$^{-/-}$ Clone A3 stably expressing H2B-mNeonGreen and mCherry-CAAX
613 with 1 μM NMS-P715 treatment. Z-max projections displayed. Frames
614 synchronized to onset of NEBD. Scale bar width = 10 μm. Images acquired on
615 Zeiss LSM 780.

616 **Figure 4.** NMS-P715 has therapeutic potential for *PRR14L* loss of function and FGFR-
617 TACC3 fusion tumors

618 (A) Flow cytometry tracking relative abundance of control and PRR14L$^{-/-}$ cells over
619 time. Cells were exposed to DMSO (1:1,000) during Days 1-3. Ribbons denote
620 standard deviation, data shown from n = 2 independent experiments.

621 (B) Flow cytometry tracking relative abundance of control and PRR14L$^{-/-}$ cells over
622 time. Cells were exposed to 1 μM NMS-P715 during Days 1-3. Ribbons denote
623 standard deviation, data shown from n = 2 independent experiments.
624 (C) Quantification of final timepoint (Day 9) of competition assay. Each dot
625 represents a single independent experiment (n = 3), and each bar represents
626 mean across independent experiments. P-value determined by one-sided
627 student's t-test, ** represents $p < 0.01$.
628 (D) Working model for PRR14L regulation of TACC3, which may potentially explain
629 *PRR14L*$^{-/-}$ phenotypes.
630 (E) Comparison of tumor cell line sensitivity between NMS-P715 and Reversine. Each point
631 represents a cancer cell line in the DepMap database. Three highlighted cell lines harbor
632 FGFR-TACC3 fusions.

633 **Figure S1.**

634 (A) Linear correlation between PRR14L-TurboID independent experiment 1 and
635 TurboID-NLS. Scatter plot displaying all proteins with >2 unique peptides
636 identified by mass spec, comparing replicate 1 against TurboID-NLS.
637 (B) Linear correlation between PRR14L-TurboID independent experiment 2 and
638 TurboID-NLS. Scatter plot displaying all proteins with >2 unique peptides
639 identified by mass spec, comparing replicate 2 against TurboID-NLS.
640 (C) Linear correlation between PRR14L-TurboID independent experiment 1 and
641 independent experiment 2. Scatter plot displaying all proteins with >2 unique
642 peptides identified by mass spec, comparing replicate 2 against replicate 1.

643 (D) Determination of filter 1 cut-off for independent experiment 1. False positive
644 protein list used was ER membrane proteins from Uniprot. False positive
645 identification plotted against log_2 ratio comparing independent experiment 1 and
646 no ligase control. Log_2 cut-off determined at a FPI = 0.03 (3% of false positive
647 proteins have log_2 ratios higher than the cut-off of 0.592).
648 (E) Determination of filter 1 cut-off for independent experiment 2. False positive
649 protein list used was ER membrane proteins from Uniprot. False positive
650 identification plotted against log_2 ratio comparing independent experiment 2 and
651 no ligase control. Log_2 cut-off determined at a FPI = 0.03 (3% of false positive
652 proteins have log_2 ratios higher than the cut-off of 0.804).
653 (F) Determination of filter 2 cut-off for independent experiment 1. False positive
654 protein list used was cell membrane proteins from Uniprot. False positive
655 identification plotted against log_2 ratio comparing independent experiment 1 and
656 spatial control. Log_2 cut-off determined at a FPI = 0.05 (5% of false positive
657 proteins have log_2 ratios higher than the cut-off of 0.335).
658 (G) Determination of filter 2 cut-off for independent experiment 2. False positive
659 protein list used was cell membrane proteins from Uniprot. False positive
660 identification plotted against log_2 ratio comparing independent experiment 2 and
661 spatial control. Log_2 cut-off determined at a FPI = 0.05 (5% of false positive
662 proteins have log_2 ratios higher than the cut-off of 0.603).
663 (H) Scatter plot displaying filter one and two for independent experiment 1.
664 (I) Scatter plot displaying filter one and two for independent experiment 2.

665 (J) Final PRR14L proximity proteome list. Most enriched protein is clearly PRR14L
666 itself.
667 (K) Final PRR14L proximity proteome list with PRR14L excluded and phosphatase
668 regulatory subunit genes highlighted, via GO annotations containing
669 "dephosphorylation."
670 (L) Final PRR14L proximity proteome list with PRR14L excluded and protein quality
671 control genes highlighted, via GO annotations containing "proteasome,"
672 "ubiquitin," and/or "protein folding."
673 (M) Final PRR14L proximity proteome list with PRR14L excluded and nuclear import
674 genes highlighted, via GO annotation containing "import into nucleus."
675 (N) Final PRR14L proximity proteome list with PRR14L excluded and mitochondrial
676 genes highlighted, via GO annotation containing "mitoch."

677

678 **Figure S2.**

679 (A) Genotyping validation of *PRR14L*$^{-/-}$ monoclonal HCT116 cells. Sanger
680 sequencing traces aligned to genomic sequence from genome assembly hg38.
681 (B) qPCR quantification of PRR14L mRNA in *PRR14L*$^{-/-}$ HCT116 cells. mRNA fold
682 change calculated via ddCt method, using *ACTB* as a control. Each dot
683 represents a single independent experiment (n = 3), and each bar represents
684 mean across independent experiments. P-value determined by one-sided
685 student's t-test, ** represents $p < 0.01$.
686 (C) Gene Set Enrichment Analysis (GSEA) of MSigDB Hallmark pathways. RNA-seq
687 data from HCT116 *PRR14L*$^{-/-}$ (KO) and NTC cells were analyzed. Genes were

688 ranked by the Wald statistic derived from DESeq2. The dot plot shows the
689 significantly enriched pathways (FDR < 0.05), faceted by activation (positive
690 Normalized Enrichment Score, NES) or suppression (negative NES) in *PRR14L*$^{-/-}$
691 cells. Dot size corresponds to the number of genes in the leading edge, and color
692 indicates the FDR-adjusted p-value.

693 (D) Differential pathway activity inference using PROGENy. VST-normalized
694 expression data was used as input to estimate the activity of 14 major signaling
695 pathways based on the expression of pathway footprint genes. The bar plot
696 displays the change in activity score (KO - NTC). Bars are colored based on
697 significance and direction of change. FDR values are indicated next to the
698 corresponding bars.

699 **Figure S3.**

700 (A) Metaphase spread counts (untreated). Histogram comparing chromosome
701 number between HCT116 NTC and HCT116 PRR14L$^{-/-}$ Clone A3. Bin width
702 displayed = 1. Data combined from n = 3 independent experiments. Total number
703 of spreads counted (NTC n = 101, PRR14L$^{-/-}$ n = 96). p-value calculated via two-
704 sided student's t-test using replicate averages.

705 (B) Metaphase spread counts (1 μM NMS-P715 treatment). Histogram comparing
706 chromosome number between HCT116 NTC and HCT116 PRR14L$^{-/-}$ Clone A3.
707 Bin width displayed = 3. Data from n = 1 independent experiment. Total number
708 of spreads counted (NTC n = 42, PRR14L$^{-/-}$ n = 42).

709 (C) Representative images comparing live cell imaging of HCT116 NTC and
710 PRR14L$^{-/-}$ Clone A3 stably expressing H2B-mNeonGreen and mCherry-CAAX

711 with 250 nM ZM 447439 treatment. Z-max projections displayed. Frames
712 synchronized to onset of NEBD. Scale bar width = 10 μm. Images acquired on
713 LSM780.
714 (D) Quantification of final timepoint (Day 9) of competition assay. Each dot
715 represents a single independent experiment (n = 2 or 1), and each bar
716 represents mean across independent experiments. DMSO values are the same
717 as independent experiments 1 and 2 from Fig. 4C.

718 **Supplementary Table 3.** Full list of proteins identified and quantified in the PRR14L
719 TurboID-MS experiment.

720

721 **References**

722 Ando, R, Shimozono, S, Ago, H, Takagi, M, Sugiyama, M, Kurokawa, H, Hirano, M,
723 Niino, Y, Ueno, G, Ishidate, F, *et al.* (2024). StayGold variants for molecular fusion and
724 membrane-targeting applications. Nat Methods 21, 648–656.

725 Baker, DJ, Jeganathan, KB, Cameron, JD, Thompson, M, Juneja, S, Kopecka, A,
726 Kumar, R, Jenkins, RB, De Groen, PC, Roche, P, *et al.* (2004). BubR1 insufficiency
727 causes early onset of aging-associated phenotypes and infertility in mice. Nat Genet 36,
728 744–749.

729 Baker, TM, Waise, S, Tarabichi, M, and Van Loo, P (2024). Aneuploidy and complex
730 genomic rearrangements in cancer evolution. Nat Cancer 5, 228–239.

731 Bakhoum, SF, and Landau, DA (2017). Chromosomal instability as a driver of tumor
732 heterogeneity and evolution. Cold Spring Harb Perspect Med 7.

733 Bakhoum, SF, Ngo, B, Laughney, AM, Cavallo, JA, Murphy, CJ, Ly, P, Shah, P, Sriram,
734 RK, Watkins, TBK, Taunk, NK, *et al.* (2018). Chromosomal instability drives metastasis
735 through a cytosolic DNA response. Nature 553, 467–472.

736 Bertomeu, T, Coulombe-Huntington, J, Chatr-aryamontri, A, Bourdages, KG, Coyaud, E,
737 Raught, B, Xia, Y, and Tyers, M (2018). A High-Resolution Genome-Wide CRISPR/Cas9
738 Viability Screen Reveals Structural Features and Contextual Diversity of the Human
739 Cell-Essential Proteome. Mol Cell Biol 38, 1–24.

740 Booth, DG, Hood, FE, Prior, IA, and Royle, SJ (2011). A TACC3/ch-TOG/clathrin
741 complex stabilises kinetochore fibres by inter-microtubule bridging. EMBO Journal 30,
742 906–919.

743 Branon, TC, Bosch, JA, Sanchez, AD, Udeshi, ND, Svinkina, T, Carr, SA, Feldman, JL,
744 Perrimon, N, and Ting, AY (2018). Efficient proximity labeling in living cells and
745 organisms with TurboID. Nat Biotechnol 36, 880–898.

746 Capelletti, M, Dodge, ME, Ercan, D, Hammerman, PS, Park, S Il, Kim, J, Sasaki, H,
747 Jablons, DM, Lipson, D, Young, L, *et al.* (2014). Identification of recurrent FGFR3-
748 TACC3 fusion oncogenes from lung adenocarcinoma. Clinical Cancer Research 20,
749 6551–6558.

750 Carneiro, BA, Elvin, JA, Kamath, SD, Ali, SM, Paintal, AS, Restrepo, A, Berry, E, Giles,
751 FJ, and Johnson, ML (2015). FGFR3-TACC3: A novel gene fusion in cervical cancer.
752 Gynecol Oncol Rep 13, 53–56.

753 Chase, A, Pellagatti, A, Singh, S, Score, J, Tapper, WJ, Lin, F, Hoade, Y, Bryant, C,
754 Trim, N, Yip, BH, *et al.* (2019). PRR14L mutations are associated with chromosome 22
755 acquired uniparental disomy, age-related clonal hematopoiesis and myeloid neoplasia.
756 Leukemia 33, 1184–1194.

757 Chase, A, Tarragona, GC, Lin, F, Yapp, S, Score, J, Bryant, C, and Cross, NCP (2023).
758 Identification of B56 α , B56 γ and BAP1 as PRR14L binding partners. 1–15.

759 Cho, KF, Branon, TC, Udeshi, ND, Myers, SA, Carr, SA, and Ting, AY (2020). Proximity
760 labeling in mammalian cells with TurboID and split-TurboID. Nat Protoc 15, 3971–3999.

761 Colombo, R, Caldarelli, M, Mennecozzi, M, Giorgini, ML, Sola, F, Cappella, P, Perrera,
762 C, Re Depaolini, S, Rusconi, L, Cucchi, U, *et al.* (2010). Targeting the mitotic checkpoint
763 for cancer therapy with NMS-P715, an inhibitor of MPS1 kinase. Cancer Res 70,
764 10255–10264.

765 Conant, D, Hsiau, T, Rossi, N, Oki, J, Maures, T, Waite, K, Yang, J, Joshi, S, Kelso, R,
766 Holden, K, *et al.* (2022). Inference of CRISPR Edits from Sanger Trace Data. CRISPR
767 Journal 5, 123–130.

768 Dobles, M, Liberal, V, Scott, ML, Benezra, R, and Sorger, PK (2000). Chromosome
769 Missegregation and Apoptosis in Mice Lacking the Mitotic Checkpoint Protein Mad2, Li
770 and Nicklas.

771 Gibson, DG, Young, L, Chuang, R-Y, Venter, JC, Hutchison, CA, and Smith, HO (2009).
772 Enzymatic assembly of DNA molecules up to several hundred kilobases. Nat Methods
773 6, 343–345.

774 Gill, KP, and Denham, M (2020). Optimized Transgene Delivery Using Third-Generation
775 Lentiviruses. Curr Protoc Mol Biol 133.

776 Gordon, DJ, Resio, B, and Pellman, D (2012). Causes and consequences of aneuploidy
777 in cancer. Nat Rev Genet 13, 189–203.

778 Hewitt, L, Tighe, A, Santaguida, S, White, AM, Jones, CD, Musacchio, A, Green, S, and
779 Taylor, SS (2010). Sustained Mps1 activity is required in mitosis to recruit O-Mad2 to the
780 Mad1-C-Mad2 core complex. Journal of Cell Biology 190, 25–34.

781 Johnson, BA, Liu, AZ, Bi, T, Dong, Y, Li, T, Zhou, D, Narkar, A, Wu, Y, Sun, SX, Larman,
782 TC, *et al.* (2024). Simple aneuploidy evades p53 surveillance and promotes niche
783 factor-independent growth in human intestinal organoids. Mol Biol Cell.

784 Katoh, Y, Michisaka, S, Nozaki, S, Funabashi, T, Hirano, T, Takei, R, and Nakayama, K
785 (2017). Practical method for targeted disruption of cilia-related genes by using
786 CRISPR/Cas9-mediated, homology-independent knock-in system. Mol Biol Cell 28,
787 898–906.

788 Koh, S-B, Mascalchi, P, Rodriguez, E, Lin, Y, Jodrell, DI, Richards, FM, and Lyons, SK
789 (2017). A quantitative FastFUCCI assay defines cell cycle dynamics at a single-cell
790 level. J Cell Sci 130, 512–520.

791 Lara-Gonzalez, P, Pines, J, and Desai, A (2021). Spindle assembly checkpoint
792 activation and silencing at kinetochores. Semin Cell Dev Biol 117, 86–98.

793 Lin, CH, Hu, CK, and Shih, HM (2010). Clathrin heavy chain mediates TACC3 targeting
794 to mitotic spindles to ensure spindle stability. Journal of Cell Biology 189, 1097–1105.

795 Narkar, A, Johnson, BA, Bharne, P, Zhu, J, Padmanaban, V, Biswas, D, Fraser, A,
796 Iglesias, PA, Ewald, AJ, and Li, R (2021). On the role of p53 in the cellular response to
797 aneuploidy. Cell Rep 34, 108892.

798 Normandin, K, Coulombe-Huntington, J, St-Denis, C, Bernard, A, Bourouh, M,
799 Bertomeu, T, Tyers, M, and Archambault, V (2023). Genetic enhancers of partial PLK1
800 inhibition reveal hypersensitivity to kinetochore perturbations. PLoS Genet 19.

801 Pemble, H, Kumar, P, van Haren, J, and Wittmann, T (2017). GSK3-mediated CLASP2
802 phosphorylation modulates kinetochore dynamics. J Cell Sci 130, 1404–1412.

803 Replogle, JM, Zhou, W, Amaro, AE, Mcfarland, JM, Villalobos-Ortiz, M, Ryan, J, Letai, A,
804 Yilmaz, O, Sheltzer, J, Lippard, SJ, *et al.* (2020). Aneuploidy increases resistance to
805 chemotherapeutics by antagonizing cell division.

806 Sanjana, NE, Shalem, O, and Zhang, F (2014). Improved vectors and genome-wide
807 libraries for CRISPR screening. Nat Methods 11, 783–784.

808 Sansregret, L, Patterson, JO, Dewhurst, S, López-García, C, Koch, A, McGranahan, N,
809 Chao, WCH, Barry, DJ, Rowan, A, Instrell, R, *et al.* (2017). APC/C dysfunction limits
810 excessive cancer chromosomal instability. Cancer Discov 7, 218–233.

811 Santaguida, S, Tighe, A, D'Alise, AM, Taylor, SS, and Musacchio, A (2010). Dissecting
812 the role of MPS1 in chromosome biorientation and the spindle checkpoint through the
813 small molecule inhibitor reversine. Journal of Cell Biology 190, 73–87.

814 Schneider, CA, Rasband, WS, and Eliceiri, KW (2012). NIH Image to ImageJ: 25 years
815 of image analysis. Nat Methods 9, 671–675.

816 Schvartzman, JM, Sotillo, R, and Benezra, R (2010). Mitotic chromosomal instability
817 and cancer: Mouse modelling of the human disease. Nat Rev Cancer 10, 102–115.

818 Singh, D, Chan, JM, Zoppoli, P, Niola, F, Sullivan, R, Castano, A, Liu, EM, Reichel, J,
819 Porrati, P, Pellegatta, S, *et al.* (2012). Transforming Fusions of FGFR and TACC Genes
820 in Human Glioblastoma. Science (1979) 337, 1231–1235.

821 Smela, MDP, Kramme, CC, Fortuna, PRJ, Adams, JL, Su, R, Dong, E, Kobayashi, M,
822 Brixi, G, Kavirayuni, VS, Tysinger, E, *et al.* (2023). Directed differentiation of human
823 iPSCs to functional ovarian granulosa-like cells via transcription factor overexpression.
824 Elife 12.

825 Still, IH, Vince, P, and Cowell, JK (1999). The Third Member of the Transforming Acidic
826 Coiled Coil-Containing Gene Family, TACC3, Maps in 4p16, Close to Translocation
827 Breakpoints in Multiple Myeloma, and Is Upregulated in Various Cancer Cell Lines.

828 Thompson, SL, and Compton, DA (2008). Examining the link between chromosomal
829 instability and aneuploidy in human cells. Journal of Cell Biology 180, 665–672.

830 Vallardi, G, Allan, LA, Crozier, L, and Saurin, AT (2019). Division of labour between
831 pp2a-b56 isoforms at the centromere and kinetochore. Elife 8, 1–25.

832 Wickham, H (2016). ggplot2 Elegant Graphics for Data Analysis Second Edition,
833 Houston.

834 Wong, S-S, Monteiro, JM, Chang, C-C, Peng, M, Mohamed, N, Steinacker, TL, Xiao, B,
835 Saurya, S, Wainman, A, and Raff, JW (2025). Centrioles generate two scaffolds with
836 distinct biophysical properties to build mitotic centrosomes. Sci Adv.

837

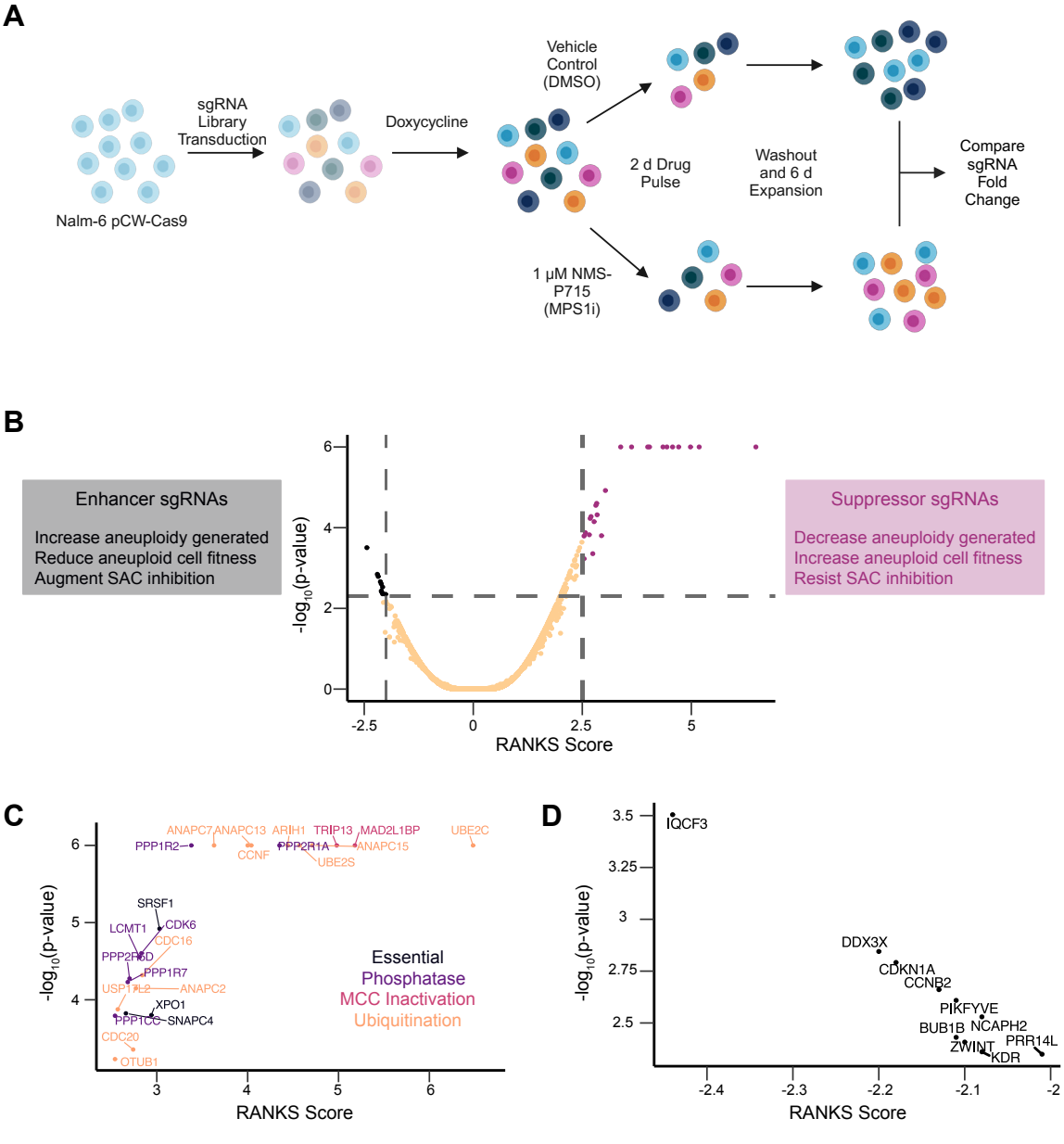
A
Nalm-6 pCW-Cas9
sgRNA Library Transduction
Doxycycline
Vehicle Control (DMSO)
2 d Drug Pulse
Washout and 6 d Expansion
1 μM NMS-P715 (MPS1i)
Compare sgRNA Fold Change
B
Enhancer sgRNAs
Increase aneuploidy generated
Reduce aneuploid cell fitness
Augment SAC inhibition
Suppressor sgRNAs
Decrease aneuploidy generated
Increase aneuploid cell fitness
Resist SAC inhibition
-log10(p-value)
RANKS Score
C
ANAPC7 ANAPC13 ARIH1 TRIP13 MAD2L1BP
PPP1R2 CCNF PPP2R1A ANAPC15 UBE2C
UBE2S
SRSF1
LCMT1 CDK6
CDC16
PPP2R6D
PPP1R7
USP17L2 ANAPC2
XPO1
PPP1CC SNAPC4
CDC20
OTUB1
Essential
Phosphatase
MCC Inactivation
Ubiquitination
-log10(p-value)
RANKS Score
D
IQCF3
DDX3X
CDKN1A
CCNB2
PIKFYVE
BUB1B NCAPH2
ZWINT PRR14L
KDR
-log10(p-value)
RANKS Score

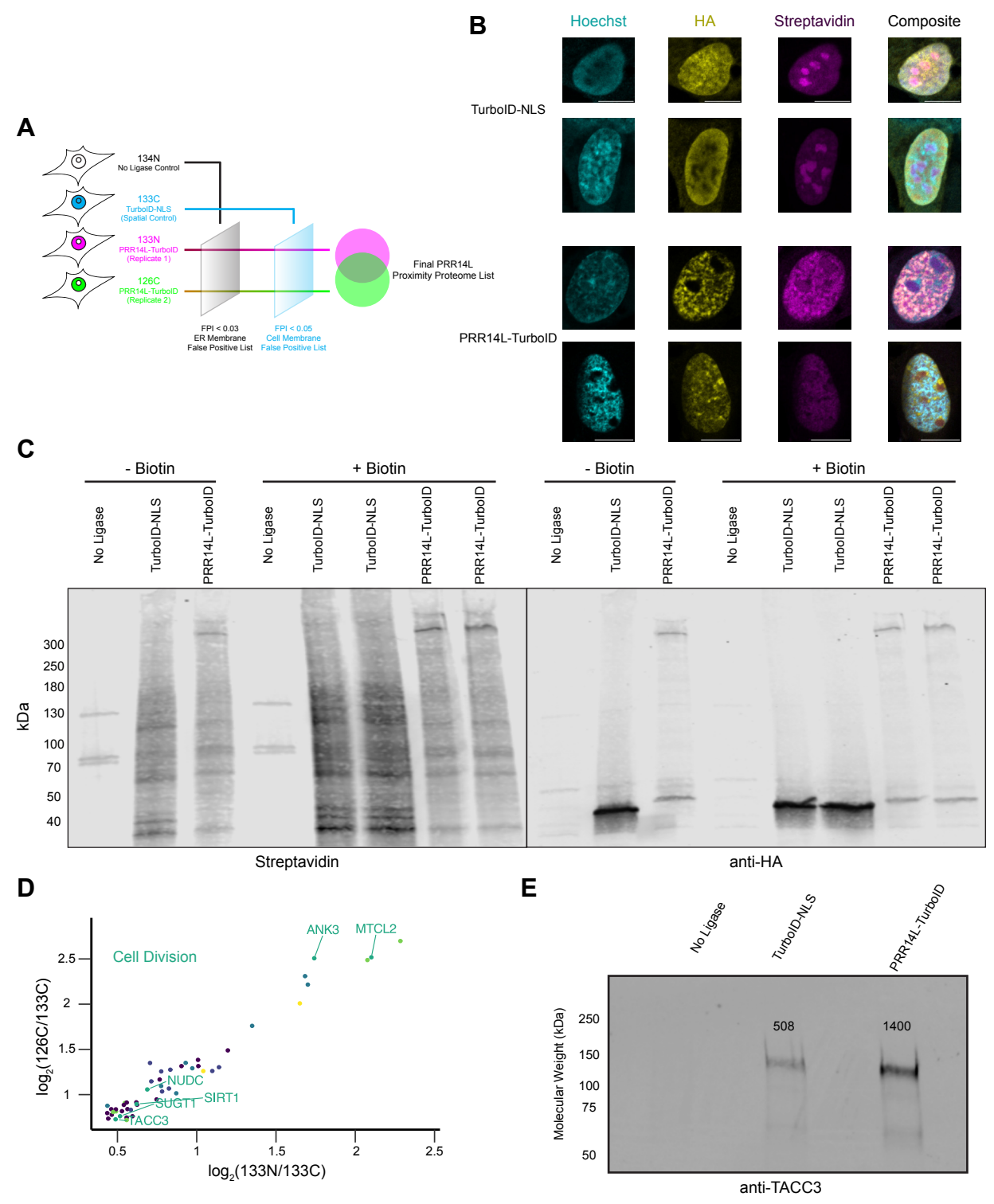
A
134N
No Ligase Control
133C
TurboID-NLS
(Spatial Control)
133N
PRR14L-TurboID
(Replicate 1)
126C
PRR14L-TurboID
(Replicate 2)
FPI < 0.03
ER Membrane
False Positive List
FPI < 0.05
Cell Membrane
False Positive List
Final PRR14L
Proximity Proteome List
B
Hoechst
HA
Streptavidin
Composite
TurboID-NLS
PRR14L-TurboID
C
- Biotin
+ Biotin
- Biotin
+ Biotin
No Ligase
TurboID-NLS
PRR14L-TurboID
kDa
300
250
180
130
100
70
50
40
Streptavidin
anti-HA
D
Cell Division
ANK3
MTCL2
NUDC
SIRT1
SUGT1
TACC3
log2(126C/133C)
log2(133N/133C)
E
No Ligase
TurboID-NLS
PRR14L-TurboID
Molecular Weight (kDa)
250
150
100
75
50
508
1400
anti-TACC3

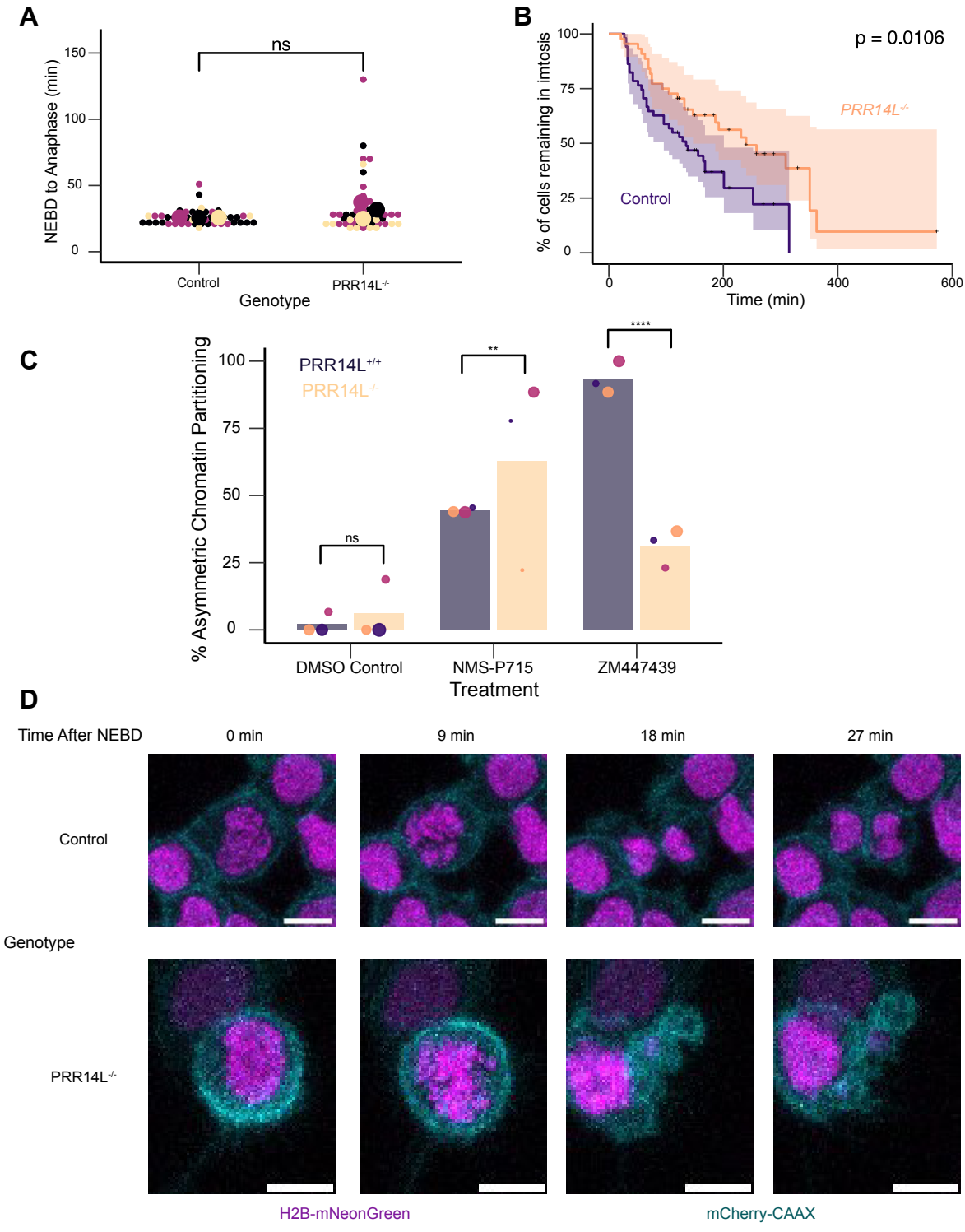
A
NEBD to Anaphase (min)
150
100
50
0
ns
Control
PRR14L-/-
Genotype
B
% of cells remaining in imtosis
100
75
50
25
0
p = 0.0106
PRR14L-/-
Control
0
200
400
600
Time (min)
C
% Asymmetric Chromatin Partitioning
100
75
50
25
0
PRR14L+/+
PRR14L-/-
ns
**
****
DMSO Control
NMS-P715
ZM447439
Treatment
D
Time After NEBD
0 min
9 min
18 min
27 min
Control
Genotype
PRR14L-/-
H2B-mNeonGreen
mCherry-CAAX

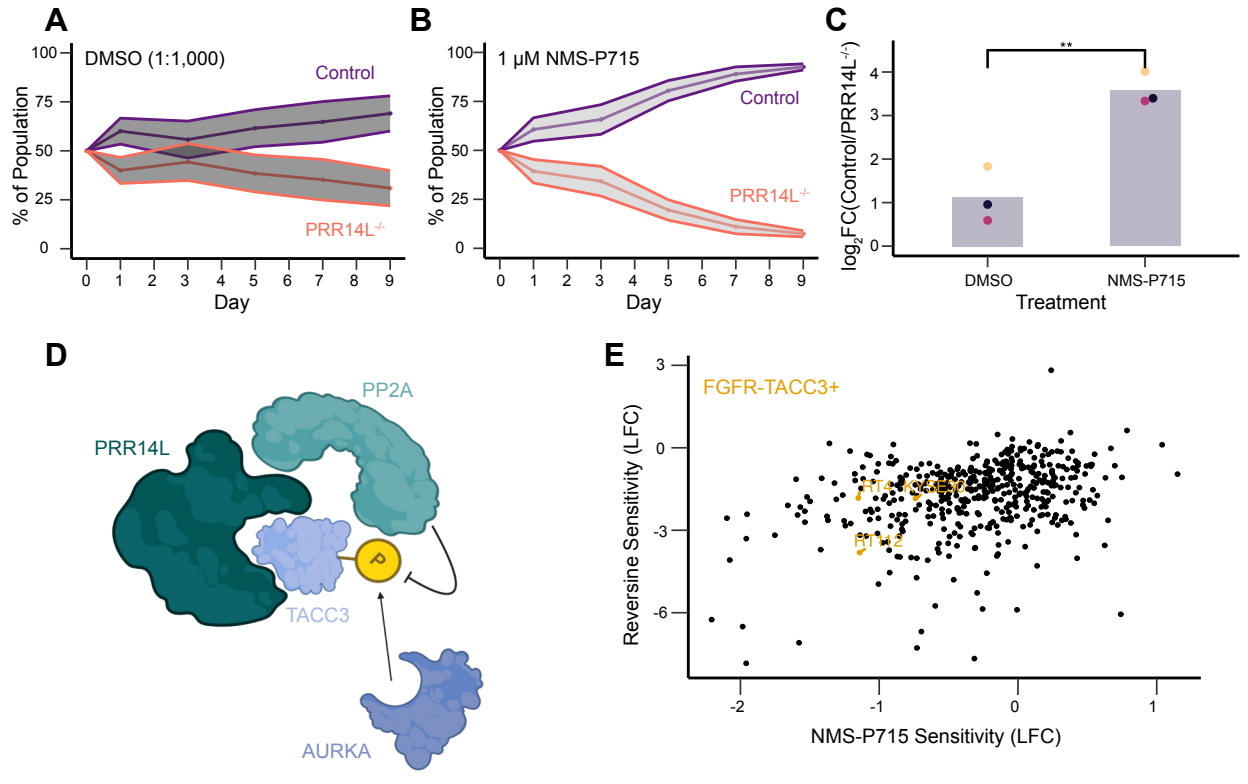
A
DMSO (1:1,000)
Control
PRR14L-/-
% of Population
Day
B
1 μM NMS-P715
Control
PRR14L-/-
% of Population
Day
C
**
log2FC(Control/PRR14L-/-)
DMSO
NMS-P715
Treatment
D
PP2A
PRR14L
TACC3
AURKA
E
FGFR-TACC3+
RT4-KMSF20
RT112
Reversine Sensitivity (LFC)
NMS-P715 Sensitivity (LFC)